

5.1 Introduction

This chapter assesses the information on past climate obtained prior to the instrumental period. The information is based on data from various paleoclimatic archives and on modelling of past climate, and updates Chapter 6 of AR4 of IPCC Working Group I (Jansen et al., 2007).

The Earth system has responded and will continue to respond to various external forcings (solar, volcanic and orbital) and to changes in atmospheric composition. Paleoclimate data and modelling provide quantitative information on the Earth system response to these forcings. Paleoclimate information facilitates understanding of Earth system feedbacks on time scales longer than a few centuries, which cannot be evaluated from short instrumental records. Past climate changes also document transitions between different climate states, including abrupt events, which occurred on time scales of decades to a few centuries. They inform about multi-centennial to millennial baseline variability, against which the recent changes can be compared to assess whether or not they are unusual.

Major progress since AR4 includes the acquisition of new and more precise information from paleoclimate archives, the synthesis of regional information, and Paleoclimate Modelling Intercomparison Project Phase III (PMIP3) and Coupled Model Intercomparison Project Phase 5 (CMIP5) simulations using the same models as for projections (see Chapter 1). This chapter assesses the understanding of past climate variations, using paleoclimate reconstructions as well as climate models of varying complexity, while the model evaluation based on paleoclimate information is covered in Chapter 9. Additional paleoclimate perspectives are included in Chapters 6, 10 and 13 (see Table 5.1).

The content of this chapter is largely restricted to topics for which substantial new information has emerged since AR4. Examples include proxy-based estimates of the atmospheric carbon dioxide (CO_2) content during the past ~65 million years (Section 5.2.2) and magnitude of sea level variations during interglacial periods (Section 5.6.2). Information from glacial climates has been included only if the underlying processes are of direct relevance for an assessment of projected climate change. The impacts of past climate changes on biological systems and past civilizations are not covered, as these topics are beyond the scope of Working Group I.

The chapter proceeds from evidence for pre-industrial changes in atmospheric composition and external solar and volcanic forcings (Section 5.2, FAQ 5.1), to global and hemispheric responses (Section 5.3). After evaluating the evidence for past changes in climate modes of variability (Section 5.4), a specific focus is given to regional changes in temperature, cryosphere and hydroclimate during the current interglacial period (Section 5.5). Sections on sea level change (Section 5.6, FAQ 5.2), abrupt climate changes (Section 5.7) and illustrations of irreversibility and recovery time scales (Section 5.8) conclude the chapter. While polar amplification of temperature changes is addressed in Box 5.1, the relationships between ice sheets, sea level, atmospheric CO_2 concentration and climate are addressed in several sections (Box 5.2, Sections 5.3.1, 5.5, and 5.8.1).

Additional information to this chapter is available in the Appendix. Processed data underlying the figures are stored in the PANGAEA database (www.pangaea.de), while model output from PMIP3 is available from pmip3.lsce.ipsl.fr. In all sections, information is structured by time, going from past to present. Table 5.1 summarizes the past periods assessed in the subsections.

5.2 Pre-Industrial Perspective on Radiative Forcing Factors

5.2.1 External Forcings

5.2.1.1 Orbital Forcing

The term 'orbital forcing' is used to denote the incoming solar radiation changes originating from variations in the Earth's orbital parameters as well as changes in its axial tilt. Orbital forcing is well known from precise astronomical calculations for the past and future (Laskar et al., 2004). Changes in eccentricity, longitude of perihelion (related to precession) and axial tilt (obliquity) (Berger and Loutre, 1991) predominantly affect the seasonal and latitudinal distribution and magnitude of solar energy received at the top of the atmosphere (AR4, Box 6.1; Jansen et al., 2007), and the durations and intensities of local seasons. Obliquity also modulates the annual mean insolation at any given latitude, with opposite effects at high and low latitudes. Orbital forcing is considered the pacemaker of transitions between glacial and interglacials (*high confidence*), although there is still no consensus on exactly how the different physical processes influenced by insolation changes interact to influence ice sheet volume (Box 5.2; Section 5.3.2). The different orbital configurations make each glacial and interglacial period unique (Yin and Berger, 2010; Tzedakis et al., 2012a). Multi-millennial trends of temperature, Arctic sea ice and glaciers during the current interglacial period, and specifically the last 2000 years, have been related to orbital forcing (Section 5.5).

5.2.1.2 Solar Forcing

Solar irradiance models (e.g., Wenzler et al., 2005) have been improved to explain better the instrumental measurements of total solar irradiance (TSI) and spectral (wavelength dependent) solar irradiance (SSI). Typical changes measured over an 11-year solar cycle are 0.1% for TSI and up to several percent for the ultraviolet (UV) part of SSI (see Section 8.4). Changes in TSI directly impact the Earth's surface (see solar Box 10.2), whereas changes in UV primarily affect the stratosphere, but can influence the tropospheric circulation through dynamical coupling (Haigh, 1996). Most models attribute all TSI and SSI changes exclusively to magnetic phenomena at the solar surface (sunspots, faculae, magnetic network), neglecting any potential internal phenomena such as changes in energy transport (see also Section 8.4). The basic concept in solar models is to divide the solar surface into different magnetic features each with a specific radiative flux. The balance of contrasting dark sunspots and bright faculae and magnetic network leads to a higher TSI value during solar cycle maxima and at most wavelengths, but some wavelengths may be out of phase with the solar cycle (Harder et al., 2009; Cahalan et al., 2010; Haigh et al., 2010). TSI and SSI are calculated by adding the radiative fluxes of all features plus the contribution from

Table 5.1 | Summary of past periods for which climate information is assessed in the various sections of this chapter and other chapters of AR5. Calendar ages are expressed in Common Era (CE), geological ages are expressed in thousand years (ka) or million years (Ma) before present (BP), with present defined as 1950. Radiocarbon-based ages are quoted as the published calibrated ages.

Time Period	Age	Chapter 5 Sections							Other Chapters
		5.2	5.3	5.4	5.5	5.6	5.7	5.8	
Holocene^a	11.65 ka ^a to present	✓	✓	✓	✓	✓			6, 9, 10
Pre-industrial period	refers to times before 1850 or 1850 values ^b								
Little Ice Age (LIA)	1450–1850 ⁱ	✓	✓	✓	✓	✓			10
Medieval Climate Anomaly (MCA) ^b	950–1250 ⁱ	✓	✓	✓	✓	✓			10
Last Millennium	1000–1999 ⁱ	✓	✓	✓	✓	✓			9, 10
Mid-Holocene (MH)	~6 ka				✓				9, 13
8.2-ka event	~8.2 ka ^a							✓	
Last Glacial Termination^c			✓			✓			6
Younger Dryas ^d	12.85–11.65 ka ^a						✓		6
Bølling-Allerød ^e	14.64–12.85 ka ^a						✓		6
Meltwater Pulse 1A (MWP-1A)	14.65–14.31 ka ^k					✓			
Heinrich stadial 1 (HS1)	~19–14.64 ka ^l						✓		
Last Glacial Maximum (LGM)	~21–19 ka ^m	✓	✓	✓					6, 9
Last Interglacial (LIG)^f	~129–116 ka ⁿ	✓	✓			✓		✓	13
Mid-Pliocene Warm Period (MPWP)	~3.3–3.0 Ma ^o	✓	✓			✓		✓	13
Early Eocene Climatic Optimum (EECO)	~52–50 Ma ^p	✓	✓						
Paleocene-Eocene Thermal Maximum (PETM)	~55.5–55.3 Ma ^q	✓	✓					✓	

Notes:

^a Also known as Marine Isotopic Stage (MIS) 1 or current interglacial.

^b Also known as Medieval Climate Optimum or the Medieval Warm Period.

^c Also known as Termination I or the Last Deglaciation. Based on sea level, Last Glacial Termination occurred between ~19 and ~6 ka.

^d Also known as Greenland Stadial GS-1.

^e Also known as Greenland Interstadial GI-a-c-e.

^f Also known as MIS5e, which overlaps with the Eemian (Shackleton et al., 2003).

^g As estimated from the Greenland ice core GICC05 chronology (Rasmussen et al., 2006; Thomas et al., 2007).

^h In this chapter, when referring to comparison of radiative forcing or climate variables, pre-industrial refers to 1850 values in accordance with Taylor et al. (2012). Otherwise it refers to an extended period of time before 1850 as stated in the text. Note that Chapter 7 uses 1750 as the reference pre-industrial period.

ⁱ Different durations are reported in the literature. In Section 5.3.5, time intervals 950–1250 and 1450–1850 are used to calculate Northern Hemisphere temperature anomalies representative of the MCA and LIA, respectively.

^j Note that CMIP5 “Last Millennium simulations” have been performed for the period 850–1850 (Taylor et al., 2012).

^k As dated on Tahiti corals (Deschamps et al., 2012).

^l The duration of Heinrich stadial 1 (e.g., Stanford et al., 2011) is longer than the associated Heinrich event, which is indicated by ice-rafted debris in deep sea sediment cores from the North Atlantic Ocean (Hemming, 2004).

^m Period based on MARGO Project Members (2009). LGM simulations are performed for 21 ka. Note that maximum continental ice extent had already occurred at 26.5 ka (Clark et al., 2009).

ⁿ Ages are maximum date for the onset and minimum age for the end from tectonically stable sites (cf. Section 5.6.2).

^o Dowsett et al. (2012).

^p Zachos et al. (2008).

^q Westerhold et al. (2007).

the magnetically inactive surface. These models can successfully reproduce the measured TSI changes between 1978 and 2003 (Balmaceda et al., 2007; Crouch et al., 2008), but not necessarily the last minimum of 2008 (Krivova et al., 2011). This approach requires detailed information of all the magnetic features and their temporal changes (Wenzler et al., 2006; Krivova and Solanki, 2008) (see Section 8.4).

The extension of TSI and SSI into the pre-satellite period poses two main challenges. First, the satellite period (since 1978) used to calibrate the solar irradiance models does not show any significant long-term trend. Second, information about the various magnetic features at the solar surface decreases back in time and must be deduced from proxies such as sunspot counts for the last 400 years and cosmogenic

radionuclides (^{10}Be and ^{14}C) for the past millennium (Muscheler et al., 2007; Delaygue and Bard, 2011) and the Holocene (Table 5.1) (Steinhilber et al., 2009; Vieira et al., 2011). ^{10}Be and ^{14}C records reflect not only solar activity, but also the geomagnetic field intensity and effects of their respective geochemical cycles and transport pathways (Pedro et al., 2011; Steinhilber et al., 2012). The corrections for these non-solar components, which are difficult to quantify, contribute to the overall error of the reconstructions (grey band in Figure 5.1c).

TSI reconstructions are characterized by distinct grand solar minima lasting 50 to 100 years (e.g., the Maunder Minimum, 1645–1715) that are superimposed upon long-term changes. Spectral analysis of TSI records reveals periodicities of 87, 104, 150, 208, 350, 510, ~980

and ~2200 years (Figure 5.1d) (Stuiver and Braziunas, 1993), but with time-varying amplitudes (Steinhilber et al., 2009; Vieira et al., 2011). All reconstructions rely ultimately on the same data (sunspots and cosmogenic radionuclides), but differ in the details of the methodologies. As a result the reconstructions agree rather well in their shape, but differ in their amplitude (Figure 5.1b) (Wang et al., 2005; Krivova et al., 2011; Lean et al., 2011; Schrijver et al., 2011) (see Section 8.4.1).

Since AR4, most recent reconstructions show a considerably smaller difference (<0.1%) in TSI between the late 20th century and the Late Maunder Minimum (1675–1715) when the sun was very quiet, compared to the often used reconstruction of Lean et al. (1995b) (0.24%) and Shapiro et al. (2011) (~0.4%). The Lean et al. (1995a) reconstruction has been used to scale solar forcing in simulations of the last millennium prior to PMIP3/CMIP5 (Table 5.A.1). PMIP3/CMIP5 last

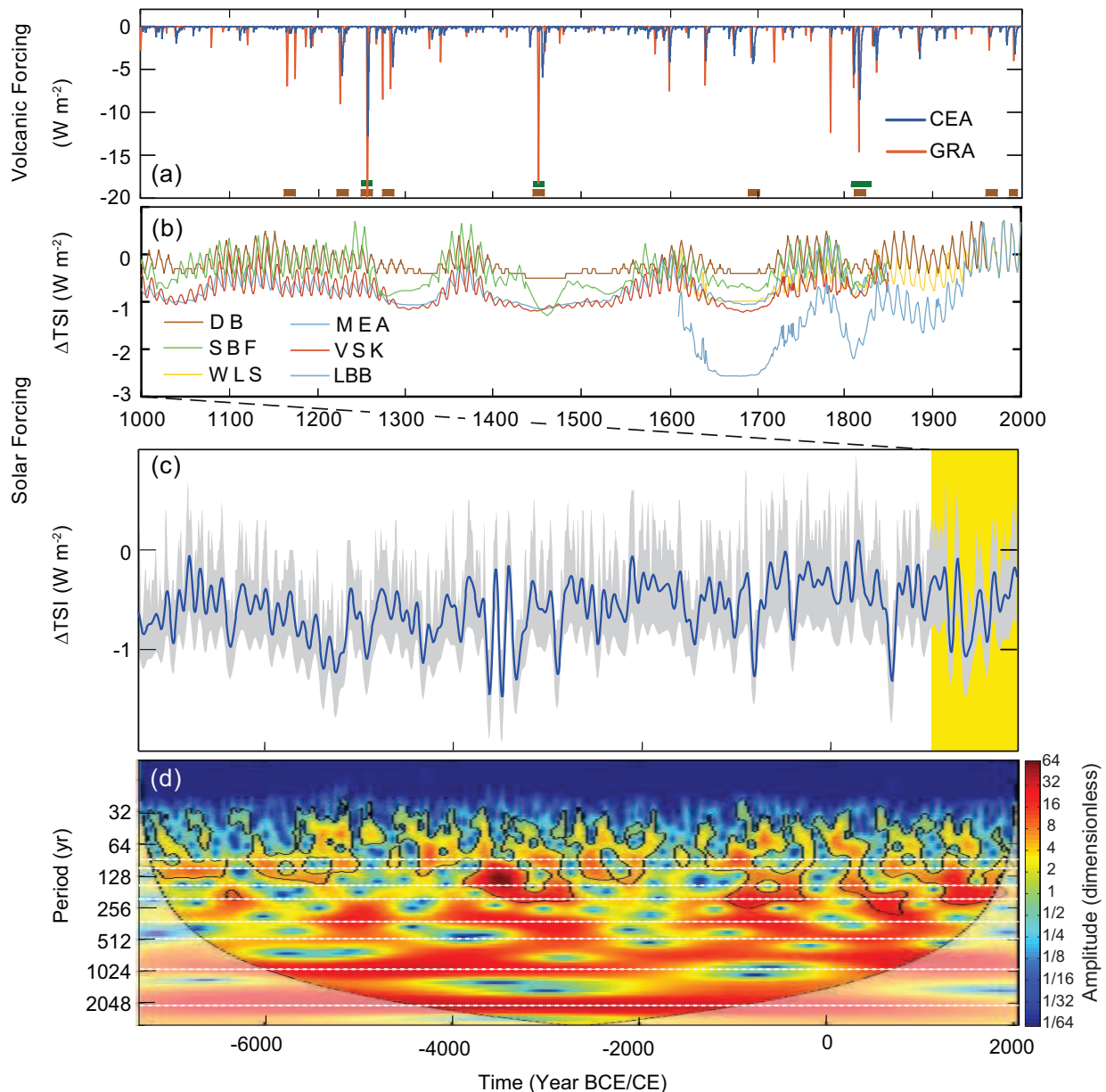


Figure 5.1 | (a) Two reconstructions of volcanic forcing for the past 1000 years derived from ice core sulphate and used for Paleoclimate Modelling Intercomparison Project Phase III (PMIP3) and Coupled Model Intercomparison Project Phase 5 (CMIP5) simulations (Schmidt et al., 2011). GRA: Gao et al. (2012); CEA: Crowley and Unterman (2013). Volcanic sulphate peaks identified from their isotopic composition as originating from the stratosphere are indicated by squares (green: Greenland; brown: Antarctica) (Baroni et al., 2008; Cole-Dai et al., 2009). (b) Reconstructed total solar irradiance (TSI) anomalies back to the year 1000. Proxies of solar activity (e.g., sunspots, ^{10}Be) are used to estimate the parameters of the models or directly TSI. All records except LBB (Lean et al., 1995b) have been used for PMIP3/CMIP5 simulations (Schmidt et al., 2011). DB: Delaygue and Bard (2011); MEA: Muscheler et al. (2007); SBF: Steinhilber et al. (2009); WLS: Wang et al. (2005); VSK: Vieira et al. (2011). For the years prior to 1600, the 11-year cycle has been added artificially to the original data with an amplitude proportional to the mean level of TSI. (c) Reconstructed TSI anomalies (100-year low-pass filtered; grey shading: 1 standard deviation uncertainty range) for the past 9300 years (Steinhilber et al., 2009). The reconstruction is based on ^{10}Be and calibrated using the relationship between instrumental data of the open magnetic field, which modulates the production of ^{10}Be , and TSI for the past four solar minima. The yellow band indicates the past 1000 years shown in more details in (a) and (b). Anomalies are relative to the 1976–2006 mean value (1366.14 W m^{-2}) of Wang et al. (2005). (d) Wavelet analysis (Torrence and Compo, 1998) of TSI anomalies from (c) with dashed white lines highlighting significant periodicities (Stuiver and Braziunas, 1993).

millennium simulations have used the weak solar forcing of recent reconstructions of TSI (Schmidt et al., 2011, 2012b) calibrated (Muscheler et al., 2007; Delaygue and Bard, 2011) or spliced (Steinhilber et al., 2009; Vieira and Solanki, 2010) to Wang et al. (2005). The larger range of past TSI variability in Shapiro et al. (2011) is not supported by studies of magnetic field indicators that suggest smaller changes over the 19th and 20th centuries (Svalgaard and Cliver, 2010; Lockwood and Owens, 2011).

Note that: (1) the recent new measurement of the absolute value of TSI and TSI changes during the past decades are assessed in Section 8.4.1.1; (2) the current state of understanding the effects of galactic cosmic rays on clouds is assessed in Sections 7.4.6 and 8.4.1.5 and (3) the use of solar forcing in simulations of the last millennium is discussed in Section 5.3.5.

5.2.1.3 Volcanic Forcing

Volcanic activity affects global climate through the radiative impacts of atmospheric sulphate aerosols injected by volcanic eruptions (see Sections 8.4.2 and 10.3.1). Quantifying volcanic forcing in the pre-satellite period is important for historical and last millennium climate simulations, climate sensitivity estimates and detection and attribution studies. Reconstructions of past volcanic forcing are based on sulphate deposition from multiple ice cores from Greenland and Antarctica, combined with atmospheric modelling of aerosol distribution and optical depth.

Since AR4, two new reconstructions of the spatial distribution of volcanic aerosol optical depth have been generated using polar ice cores, spanning the last 1500 years (Gao et al., 2008, 2012) and 1200 years (Crowley and Unterman, 2013) (Figure 5.1a). Although the relative size of eruptions for the past 700 years is generally consistent among these and earlier studies (Jansen et al., 2007), they differ in the absolute amplitude of peaks. There are also differences in the reconstructions of Icelandic eruptions, with an ongoing debate on the magnitude of stratospheric inputs for the 1783 Laki eruption (Thordarson and Self, 2003; Wei et al., 2008; Lanciki et al., 2012; Schmidt et al., 2012a). The recurrence time of past large volcanic aerosol injections (eruptions changing the radiative forcing (RF) by more than 1 W m^{-2}) varies from 3 to 121 years, with long-term mean value of 35 years (Gao et al., 2012) and 39 years (Crowley and Unterman, 2013), and only two or three periods of 100 years without such eruptions since 850.

Hegerl et al. (2006) estimated the uncertainty of the RF for a given volcanic event to be approximately 50%. Differences between reconstructions (Figure 5.1a) arise from different proxy data, identification of the type of injection, methodologies to estimate particle distribution and optical depth (Kravitz and Robock, 2011), and parameterization of scavenging for large events (Timmreck et al., 2009). Key limitations are associated with ice core chronologies (Plummer et al., 2012; Sigl et al., 2013), and deposition patterns (Moore et al., 2012).

A new independent methodology has recently been developed to distinguish between tropospheric and stratospheric volcanic aerosol deposits (Baroni et al., 2007). The stratospheric character of several large eruptions has started to be assessed from Greenland and/or

Antarctic ice core sulphur isotope data (Baroni et al., 2008; Cole-Dai et al., 2009; Schmidt et al., 2012b).

The use of different volcanic forcing reconstructions in pre-PMIP3/CMIP5 (see AR4 Chapter 6) and PMIP3/CMIP5 last millennium simulations (Schmidt et al., 2011) (Table 5.A.1), together with the methods used to implement these volcanic indices with different representations of aerosols in climate models, is a source of uncertainty in model intercomparisons. The impact of volcanic forcing on climate variations of the last millennium climate is assessed in Sections 5.3.5, 5.4, 5.5.1 and 10.7.1.

5.2.2 Radiative Perturbations from Greenhouse Gases and Dust

5.2.2.1 Atmospheric Concentrations of Carbon Dioxide, Methane and Nitrous Oxide from Ice Cores

Complementing instrumental data, air enclosed in polar ice provides a direct record of past atmospheric well-mixed greenhouse gas (WMGHG) concentrations albeit smoothed by firn diffusion (Joos and Spahni, 2008; Köhler et al., 2011). Since AR4, the temporal resolution of ice core records has been enhanced (MacFarling Meure et al., 2006; Ahn and Brook, 2008; Louergue et al., 2008; Lüthi et al., 2008; Mischler et al., 2009; Schilt et al., 2010; Ahn et al., 2012; Bereiter et al., 2012). During the pre-industrial part of the last 7000 years, millennial (20 ppm CO_2 , 125 ppb CH_4) and centennial variations (up to 10 ppm CO_2 , 40 ppb CH_4 and 10 ppb N_2O) are recorded (see Section 6.2.2 and Figure 6.6). Significant centennial variations in CH_4 during the last glacial occur in phase with Northern Hemisphere (NH) rapid climate changes, while millennial CO_2 changes coincide with their Southern Hemisphere (SH) bipolar seesaw counterpart (Ahn and Brook, 2008; Louergue et al., 2008; Lüthi et al., 2008; Grachev et al., 2009; Capron et al., 2010b; Schilt et al., 2010; Bereiter et al., 2012).

Long-term records have been extended from 650 ka in AR4 to 800 ka (Figures 5.2 and 5.3) (Louergue et al., 2008; Lüthi et al., 2008; Schilt et al., 2010). During the last 800 ka, the pre-industrial ice core WMGHG concentrations stay within well-defined natural limits with maximum interglacial concentrations of approximately 300 ppm, 800 ppb and 300 ppb for CO_2 , CH_4 and N_2O , respectively, and minimum glacial concentrations of approximately 180 ppm, 350 ppb, and 200 ppb. The new data show lower than pre-industrial (280 ppm) CO_2 concentrations during interglacial periods from 800 to 430 ka (MIS19 to MIS13) (Figure 5.3). It is a fact that present-day (2011) concentrations of CO_2 (390.5 ppm), CH_4 (1803 ppb) and N_2O (324 ppm) (Annex II) exceed the range of concentrations recorded in the ice core records during the past 800 ka. With *very high confidence*, the rate of change of the observed anthropogenic WMGHG rise and its RF is unprecedented with respect to the highest resolution ice core record back to 22 ka for CO_2 , CH_4 and N_2O , accounting for the smoothing due to ice core enclosure processes (Joos and Spahni, 2008; Schilt et al., 2010). There is *medium confidence* that the rate of change of the observed anthropogenic WMGHG rise is also unprecedented with respect to the lower resolution records of the past 800 ka.

Progress in understanding the causes of past WMGHG variations is reported in Section 6.2.

Frequently Asked Questions

FAQ 5.1 | Is the Sun a Major Driver of Recent Changes in Climate?

Total solar irradiance (TSI, Chapter 8) is a measure of the total energy received from the sun at the top of the atmosphere. It varies over a wide range of time scales, from billions of years to just a few days, though variations have been relatively small over the past 140 years. Changes in solar irradiance are an important driver of climate variability (Chapter 1; Figure 1.1) along with volcanic emissions and anthropogenic factors. As such, they help explain the observed change in global surface temperatures during the instrumental period (FAQ 5.1, Figure 1; Chapter 10) and over the last millennium. While solar variability may have had a discernible contribution to changes in global surface temperature in the early 20th century, it cannot explain the observed increase since TSI started to be measured directly by satellites in the late 1970s (Chapters 8, 10).

The Sun's core is a massive nuclear fusion reactor that converts hydrogen into helium. This process produces energy that radiates throughout the solar system as electromagnetic radiation. The amount of energy striking the top of Earth's atmosphere varies depending on the generation and emission of electromagnetic energy by the Sun and on the Earth's orbital path around the Sun.

Satellite-based instruments have directly measured TSI since 1978, and indicate that on average, $\sim 1361 \text{ W m}^{-2}$ reaches the top of the Earth's atmosphere. Parts of the Earth's surface and air pollution and clouds in the atmosphere act as a mirror and reflect about 30% of this power back into space. Higher levels of TSI are recorded when the Sun is more active. Irradiance variations follow the roughly 11-year sunspot cycle: during the last cycles, TSI values fluctuated by an average of around 0.1%.

For pre-satellite times, TSI variations have to be estimated from sunspot numbers (back to 1610), or from radioisotopes that are formed in the atmosphere, and archived in polar ice and tree rings. Distinct 50- to 100-year periods of very low solar activity—such as the Maunder Minimum between 1645 and 1715—are commonly referred to as grand solar minima. Most estimates of TSI changes between the Maunder Minimum and the present day are in the order of 0.1%, similar to the amplitude of the 11-year variability.

How can solar variability help explain the observed global surface temperature record back to 1870? To answer this question, it is important to understand that other climate drivers are involved, each producing characteristic patterns of regional climate responses. However, it is the combination of them all that causes the observed climate change. Solar variability and volcanic eruptions are natural factors. Anthropogenic (human-produced) factors, on the other hand, include changes in the concentrations of greenhouse gases, and emissions of visible air pollution (aerosols) and other substances from human activities. 'Internal variability' refers to fluctuations within the climate system, for example, due to weather variability or phenomena like the El Niño-Southern Oscillation.

The relative contributions of these natural and anthropogenic factors change with time. FAQ 5.1, Figure 1 illustrates those contributions based on a very simple calculation, in which the mean global surface temperature variation represents the sum of four components linearly related to solar, volcanic, and anthropogenic forcing, and to internal variability. Global surface temperature has increased by approximately 0.8°C from 1870 to 2010 (FAQ 5.1, Figure 1a). However, this increase has not been uniform: at times, factors that cool the Earth's surface—volcanic eruptions, reduced solar activity, most anthropogenic aerosol emissions—have outweighed those factors that warm it, such as greenhouse gases, and the variability generated within the climate system has caused further fluctuations unrelated to external influences.

The solar contribution to the record of global surface temperature change is dominated by the 11-year solar cycle, which can explain global temperature fluctuations up to approximately 0.1°C between minima and maxima (FAQ 5.1, Figure 1b). A long-term increasing trend in solar activity in the early 20th century may have augmented the warming recorded during this interval, together with internal variability, greenhouse gas increases and a hiatus in volcanism. However, it cannot explain the observed increase since the late 1970s, and there was even a slight decreasing trend of TSI from 1986 to 2008 (Chapters 8 and 10).

Volcanic eruptions contribute to global surface temperature change by episodically injecting aerosols into the atmosphere, which cool the Earth's surface (FAQ 5.1, Figure 1c). Large volcanic eruptions, such as the eruption of Mt. Pinatubo in 1991, can cool the surface by around 0.1°C to 0.3°C for up to three years. *(continued on next page)*

FAQ 5.1 (continued)

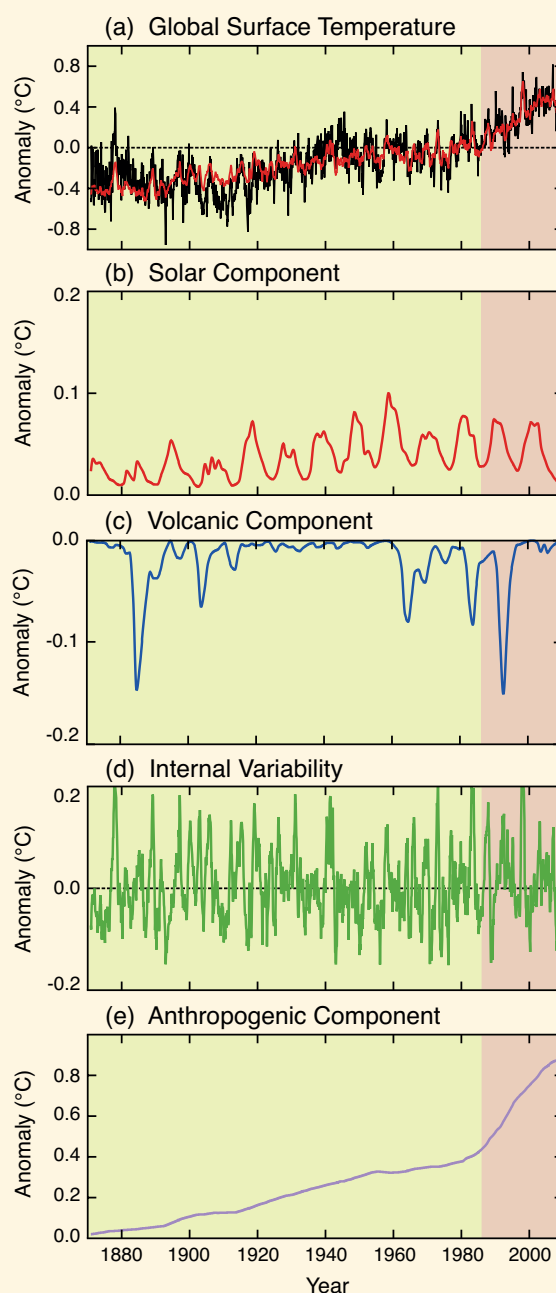
The most important component of internal climate variability is the El Niño Southern Oscillation, which has a major effect on year-to-year variations of tropical and global mean temperature (FAQ 5.1, Figure 1d). Relatively high annual temperatures have been encountered during El Niño events, such as in 1997–1998.

The variability of observed global surface temperatures from 1870 to 2010 (Figure 1a) reflects the combined influences of natural (solar, volcanic, internal; FAQ 5.1, Figure 1b–d) factors, superimposed on the multi-decadal warming trend from anthropogenic factors (FAQ 5.1, Figure 1e).

Prior to 1870, when anthropogenic emissions of greenhouse gases and aerosols were smaller, changes in solar and volcanic activity and internal variability played a more important role, although the specific contributions of these individual factors to global surface temperatures are less certain. Solar minima lasting several decades have often been associated with cold conditions. However, these periods are often also affected by volcanic eruptions, making it difficult to quantify the solar contribution.

At the regional scale, changes in solar activity have been related to changes in surface climate and atmospheric circulation in the Indo-Pacific, Northern Asia and North Atlantic areas. The mechanisms that amplify the regional effects of the relatively small fluctuations of TSI in the roughly 11-year solar cycle involve dynamical interactions between the upper and the lower atmosphere, or between the ocean sea surface temperature and atmosphere, and have little effect on global mean temperatures (see Box 10.2).

Finally, a decrease in solar activity during the past solar minimum a few years ago (FAQ 5.1, Figure 1b) raises the question of its future influence on climate. Despite uncertainties in future solar activity, there is *high confidence* that the effects of solar activity within the range of grand solar maxima and minima will be much smaller than the changes due to anthropogenic effects.



FAQ 5.1, Figure 1 | Global surface temperature anomalies from 1870 to 2010, and the natural (solar, volcanic, and internal) and anthropogenic factors that influence them. (a) Global surface temperature record (1870–2010) relative to the average global surface temperature for 1961–1990 (black line). A model of global surface temperature change (a: red line) produced using the sum of the impacts on temperature of natural (b, c, d) and anthropogenic factors (e). (b) Estimated temperature response to solar forcing. (c) Estimated temperature response to volcanic eruptions. (d) Estimated temperature variability due to internal variability, here related to the El Niño–Southern Oscillation. (e) Estimated temperature response to anthropogenic forcing, consisting of a warming component from greenhouse gases, and a cooling component from most aerosols.

5.2.2.2 Atmospheric Carbon Dioxide Concentrations from Geological Proxy Data

Geological proxies provide indirect information on atmospheric CO₂ concentrations for time intervals older than those covered by ice core records (see Section 5.2.2.1). Since AR4, the four primary proxy CO₂ methods have undergone further development (Table 5.A.2). A reassessment of biological respiration and carbonate formation has reduced CO₂ reconstructions based on fossil soils by approximately 50% (Breecker et al., 2010). Bayesian statistical techniques for calibrating leaf stomatal density reconstructions produce consistently higher CO₂ estimates than previously assessed (Beerling et al., 2009), resulting in more convergence between estimates from these two terrestrial proxies. Recent CO₂ reconstructions using the boron isotope proxy provide an improved understanding of foraminifer species effects and evolution of seawater alkalinity (Hönisch and Hemming, 2005) and seawater boron isotopic composition (Foster et al., 2012). Quantification of the phytoplankton cell-size effects on carbon isotope fractionation has also improved the consistency of the alkenone method (Henderiks and Pagani, 2007). These proxies have also been applied more widely and at higher temporal resolution to a range of geological archives, resulting in an increased number of atmospheric CO₂ estimates since 65 Ma (Beerling and Royer, 2011). Although there is improved consensus between the proxy CO₂ estimates, especially the marine proxy estimates, a significant degree of variation among the different techniques remains. All four techniques have been included in the assessment, as there is insufficient knowledge to discriminate between different proxy estimates on the basis of confidence (assessed in Table 5.A.2).

In the time interval between 65 and 23 Ma, all proxy estimates of CO₂ concentration span a range of 300 ppm to 1500 ppm (Figure 5.2). An independent constraint on Early Eocene atmospheric CO₂ concentration is provided by the occurrence of the sodium carbonate mineral nahcolite, in about 50 Ma lake sediments, which precipitates in association with halite at the sediment–water interface only at CO₂ levels >1125 ppm (Lowenstein and Demicco, 2006), and thus provides a potential lower bound for atmospheric concentration (*medium confidence*) during the warmest period of the last 65 Ma, the Early Eocene Climatic Optimum (EECO; 52 to 50 Ma; Table 5.1), which is inconsistent with lower estimates from stomata and paleosoils. Although the reconstructions indicate a general decrease in CO₂ concentrations since about 50 Ma (Figure 5.2), the large scatter of proxy data precludes a robust assessment of the second-order variation around this overall trend.

Since 23 Ma, CO₂ proxy estimates are at pre-industrial levels with exception of the Middle Miocene climatic optimum (17 to 15 Ma) and the Pliocene (5.3 to 2.6 Ma), which have higher concentrations. Although new CO₂ reconstructions for the Pliocene based on marine proxies have produced consistent estimates mostly in the range 350 ppm to 450 ppm (Pagani et al., 2010; Seki et al., 2010; Bartoli et al., 2011), the uncertainties associated with these marine estimates remain difficult to quantify. Several boron-derived data sets agree within error (± 25 ppm) with the ice core records (Foster, 2008; Hönisch et al., 2009), but alkenone data for the ice core period are outside the error limits (Figure 5.2). We conclude that there is *medium confidence* that CO₂ levels were above pre-industrial interglacial concentration (~ 280 ppm)

and did not exceed ~ 450 ppm during the Pliocene, with interglacial values in the upper part of that range between 350 and 450 ppm.

5.2.2.3 Past Changes in Mineral Dust Aerosol Concentrations

Past changes in mineral dust aerosol (MDA) are important for estimates of climate sensitivity (see Section 5.3.3) and for its supply of nutrients, especially iron to the Southern Ocean (see Section 6.2). MDA concentration is controlled by variations in dust sources, and by changes in atmospheric circulation patterns acting on its transport and lifetime.

Since AR4, new records of past MDA flux have been obtained from deep-sea sediment and ice cores. A 4 million-year MDA-flux reconstruction from the Southern Ocean (Figure 5.2) implies reduced dust generation and transport during the Pliocene compared to Holocene levels, followed by a significant rise around 2.7 Ma when NH ice volume increased (Martinez-Garcia et al., 2011). Central Antarctic ice core records show that local MDA deposition fluxes are ~ 20 times higher during glacial compared to interglacial periods (Fischer et al., 2007; Lambert et al., 2008; Petit and Delmonte, 2009). This is due to enhanced dust production in southern South America and perhaps Australia (Gaiero, 2007; De Deckker et al., 2010; Gabrielli et al., 2010; Martinez-Garcia et al., 2011; Wegner et al., 2012). The impact of changes in MDA lifetime (Petit and Delmonte, 2009) on dust fluxes in Antarctica remains uncertain (Fischer et al., 2007; Wolff et al., 2010). Equatorial Pacific glacial–interglacial MDA fluxes co-vary with Antarctic records, but with a glacial–interglacial ratio in the range of approximately three to four (Winckler et al., 2008), attributed to enhanced dust production from Asian and northern South American sources in glacial times (Maher et al., 2010). The dominant dust source regions (e.g., North Africa, Arabia and Central Asia) show complex patterns of variability (Roberts et al., 2011). A glacial increase of MDA source strength by a factor of 3 to 4 requires low vegetation cover, seasonal aridity, and high wind speeds (Fischer et al., 2007; McGee et al., 2010). In Greenland ice cores, MDA ice concentrations are higher by a factor of 100 and deposition fluxes by a factor 20 during glacial periods (Ruth et al., 2007). This is due mainly to changes in the dust sources for Greenland (Asian desert areas), increased gustiness (McGee et al., 2010) and atmospheric lifetime and transport of MDA (Fischer et al., 2007). A strong coherence is observed between dust in Greenland ice cores and aeolian deposition in European loess formations (Antoine et al., 2009).

Global data synthesis shows two to four times more dust deposition at the Last Glacial Maximum (LGM; Table 5.1) than today (Derbyshire, 2003; Maher et al., 2010). Based on data–model comparisons, estimates of global mean LGM dust RF vary from -3 W m^{-2} to $+0.1 \text{ W m}^{-2}$, due to uncertainties in radiative properties. The best estimate value remains at -1 W m^{-2} as in AR4 (Claquin et al., 2003; Mahowald et al., 2006, 2011; Patadia et al., 2009; Takemura et al., 2009; Yue et al., 2010). Models may underestimate the MDA RF at high latitudes (Lambert et al., 2013).

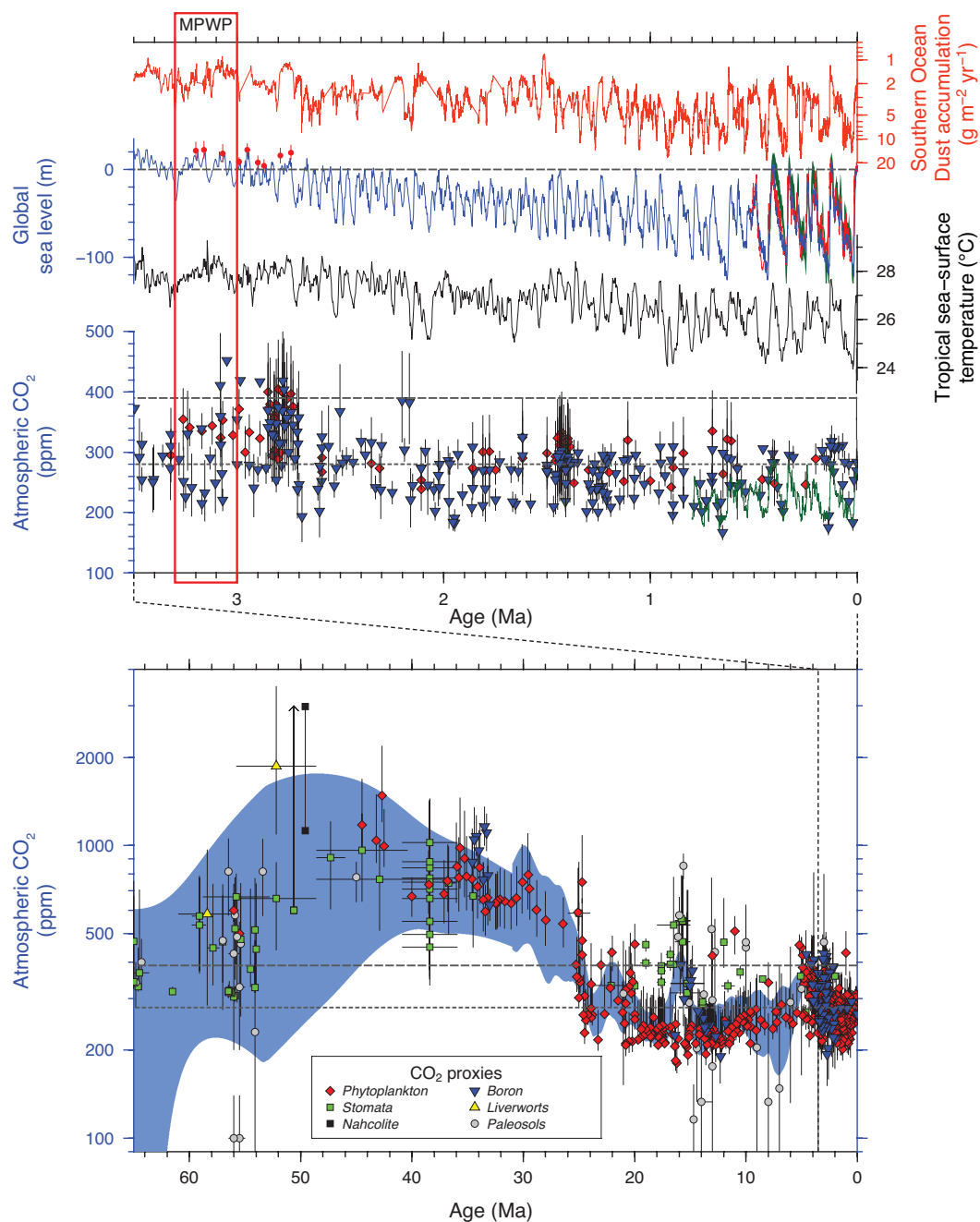


Figure 5.2 | (Top) Orbital-scale Earth system responses to radiative forcings and perturbations from 3.5 Ma to present. Reconstructed dust mass accumulation rate is from the Atlantic sector of the Southern Ocean (red) (Martinez-Garcia et al., 2011). Sea level curve (blue) is the stacked $\delta^{18}\text{O}$ proxy for ice volume and ocean temperature (Lisiecki and Raymo, 2005) calibrated to global average eustatic sea level (Naish and Wilson, 2009; Miller et al., 2012a). Also shown are global eustatic sea level reconstructions for the last 500 kyr based on sea level calibration of the $\delta^{18}\text{O}$ curve using dated coral shorelines (green line; Waelbroeck et al., 2002) and the Red Sea isotopic reconstruction (red line; Rohling et al., 2009). Weighted mean estimates (2 standard deviation uncertainty) for far-field reconstructions of eustatic peaks are shown for mid-Pliocene interglacials (red dots; Miller et al., 2012a). The dashed horizontal line represents present-day sea level. Tropical sea surface temperature (black line) based on a stack of four alkenone-based sea surface temperature reconstructions (Herbert et al., 2010). Atmospheric carbon dioxide (CO_2) measured from Antarctic ice cores (green line, Petit et al., 1999; Siegenthaler et al., 2005; Lüthi et al., 2008), and estimates of CO_2 from boron isotopes ($\delta^{11}\text{B}$) in foraminifera in marine sediments (blue triangles; Hönisch et al., 2009; Seki et al., 2010; Bartoli et al., 2011), and phytoplankton alkenone-derived carbon isotope proxies (red diamonds; Pagani et al., 2010; Seki et al., 2010), plotted with 2 standard deviation uncertainty. Present (2012) and pre-industrial CO_2 concentrations are indicated with long-dashed and short-dashed grey lines, respectively. (Bottom) Concentration of atmospheric CO_2 for the last 65 Ma is reconstructed from marine and terrestrial proxies (Cerling, 1992; Freeman and Hayes, 1992; Koch et al., 1992; Stott, 1992; van der Burgh et al., 1993; Sinha and Stott, 1994; Kürschner, 1996; McElwain, 1998; Ekart et al., 1999; Pagani et al., 1999a, 1999b, 2005a, 2005b, 2010, 2011; Kürschner et al., 2001, 2008; Royer et al., 2001a, 2001b; Beerling et al., 2002, 2009; Beerling and Royer, 2002; Nordt et al., 2002; Greenwood et al., 2003; Royer, 2003; Lowenstein and Demicco, 2006; Fletcher et al., 2008; Pearson et al., 2009; Retallack, 2009b, 2009a; Tripathi et al., 2009; Seki et al., 2010; Smith et al., 2010; Bartoli et al., 2011; Doria et al., 2011; Foster et al., 2012). Individual proxy methods are colour-coded (see also Table A5.1). The light blue shading is a 1-standard deviation uncertainty band constructed using block bootstrap resampling (Mudelsee et al., 2012) for a kernel regression through all the data points with a bandwidth of 8 Myr prior to 30 Ma, and 1 Myr from 30 Ma to present. Most of the data points for CO_2 proxies are based on duplicate and multiple analyses. The red box labelled MPWP represents the mid-Pliocene Warm Period (3.3 to 3.0 Ma; Table 5.1).

Box 5.1 | Polar Amplification

Polar amplification occurs if the magnitude of zonally averaged surface temperature change at high latitudes exceeds the globally averaged temperature change, in response to climate forcings and on time scales greater than the annual cycle. Polar amplification is of global concern due to the potential effects of future warming on ice sheet stability and, therefore, global sea level (see Sections 5.6.1, 5.8.1 and Chapter 13) and carbon cycle feedbacks such as those linked with permafrost melting (see Chapter 6).

Some external climate forcings have an enhanced radiative impact at high latitudes, such as orbital forcing (Section 5.2.1.1), or black carbon (Section 8.3.4). Here, we focus on the latitudinal response of surface temperature to CO₂ perturbations. The magnitude of polar amplification depends on the relative strength and duration of different climate feedbacks, which determine the transient and equilibrium response to external forcings. This box first describes the different feedbacks operating in both polar regions, and then contrasts polar amplification depicted for past high CO₂ and low CO₂ climates with projected temperature patterns for the RCP8.5 future greenhouse gas (WMGHG) emission scenario.

In the Arctic, the sea ice/ocean surface albedo feedback plays an important role (Curry et al., 1995; Serreze and Barry, 2011). With retreating sea ice, surface albedo decreases, air temperatures increase and the ocean can absorb more heat. The resulting ocean warming contributes to further sea ice melting. The sea ice/ocean surface albedo feedback can exhibit threshold behaviour when temperatures exceed the freezing point of sea ice. This may also translate into a strong seasonality of the response characteristics. Other feedbacks, including water vapour and cloud feedbacks have been suggested as important amplifiers of Arctic climate change (Vavrus, 2004; Abbot and Tziperman, 2008, 2009; Graversen and Wang, 2009; Lu and Cai, 2009; Screen and Simmonds, 2010; Bintanja et al., 2011). In continental Arctic regions with seasonal snow cover, changes in radiative forcing (RF) can heavily influence snow cover (Ghatak et al., 2010), and thus surface albedo. Other positive feedbacks operating on time scales of decades-to-centuries in continental high-latitude regions are associated with surface vegetation changes (Bhatt et al., 2010) and thawing permafrost (e.g., Walter et al., 2006). On glacial-to-interglacial time scales, the very slow ice sheet–albedo response to external forcings (see Box 5.2) is a major contributor to polar amplification in the Northern Hemisphere.

An amplified response of Southern Ocean sea surface temperature (SST) to radiative perturbations also emerges from the sea ice–albedo feedback. However, in contrast to the Arctic Ocean, which in parts is highly stratified, mixed-layer depths in the Southern Ocean typically exceed several hundreds of meters, which allows the ocean to take up vast amounts of heat (Böning et al., 2008; Gille, 2008; Sokolov and Rintoul, 2009) and damp the SST response to external forcing. This process, and the presence of the ozone hole over the Antarctic ice sheet (Thompson and Solomon, 2002, 2009), can affect the transient response of surface warming of the Southern Ocean and Antarctica, and lead to different patterns of future polar amplification on multi-decadal to multi-centennial time scales. In response to rapid atmospheric CO₂ changes, climate models indeed project an asymmetric warming between the Arctic and Southern Oceans, with an earlier response in the Arctic and a delayed response in the Southern Ocean (Section 12.4.3). Above the Antarctic ice sheet, however, surface air temperature can respond quickly to radiative perturbations owing to the limited role of latent heat flux in the surface energy budget of Antarctica.

These differences in transient and equilibrium responses of surface temperatures on Antarctica, the Southern Ocean and over continents and oceans in the Arctic domain can explain differences in the latitudinal temperature patterns depicted in Box 5.1, Figure 1 for past periods (equilibrium response) and future projections (transient response).

Box 5.1, Figure 1 illustrates the polar amplification phenomenon for three different periods of the Earth's climate history using temperature reconstructions from natural archives and climate model simulations for: (i) the Early Eocene Climatic Optimum (EECO, 54 to 48 Ma) characterised by CO₂ concentrations of 1000 to 2000 ppm (Section 5.2.2.2) and the absence of continental ice sheets; (ii) the mid-Pliocene Warm Period (MPWP, 3.3 to 3.0 Ma), characterized by CO₂ concentrations in the range of 350 to 450 ppm (Section 5.2.2.2) and reduced Greenland and Antarctic ice sheets compared to today (see Section 5.6.1), (iii) the Last Glacial Maximum (LGM, 21 to 19 ka), characterized by CO₂ concentrations around 200 ppm and large continental ice sheets covering northern Europe and North America.

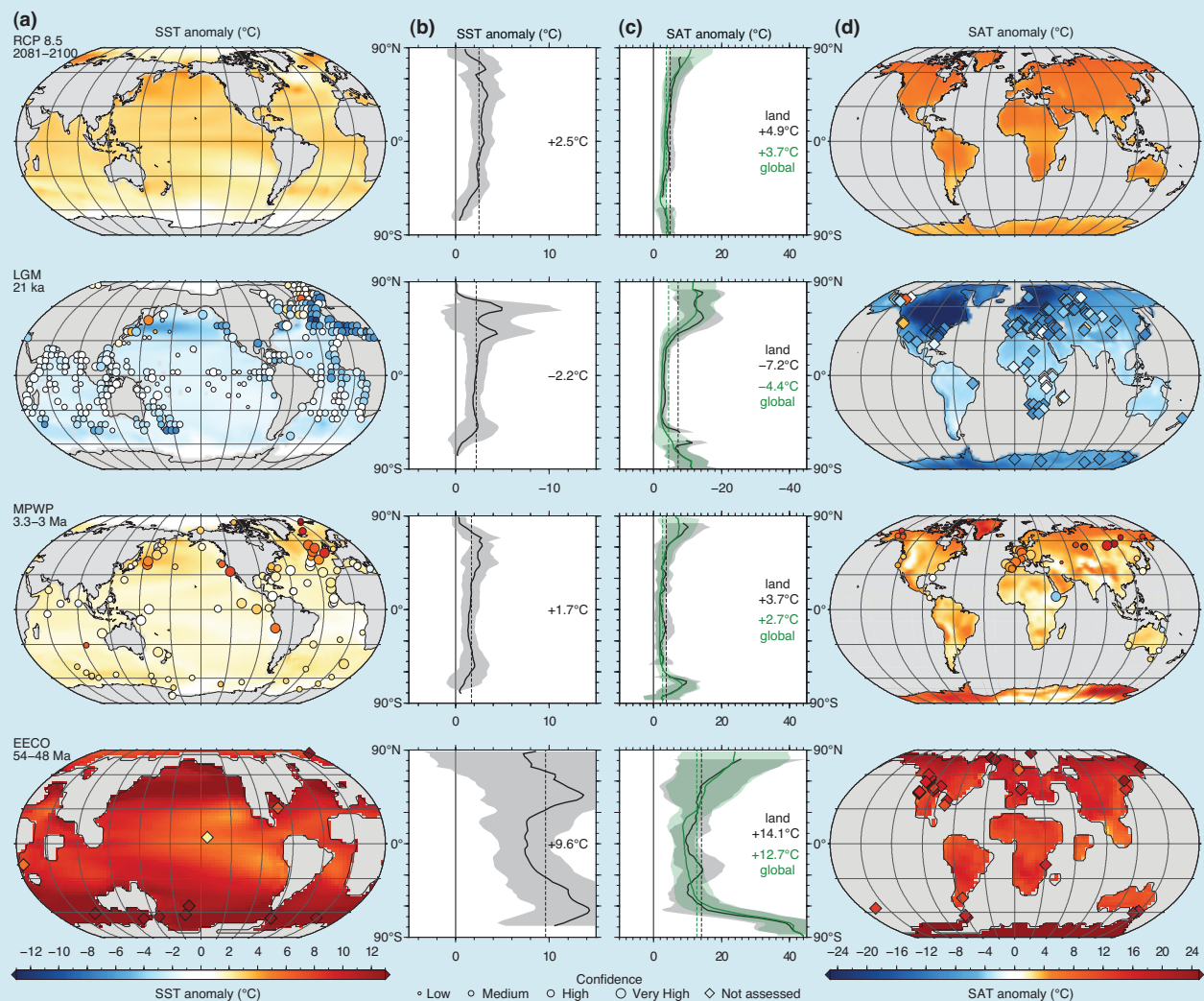
Throughout all three time periods, reconstructions and simulations reveal Arctic and Antarctic surface air temperature amplification of up to two times the global mean (Box 5.1, Figure 1c, d), and this bipolar amplification appears to be a robust feature of the equilibrium Earth system response to changes of CO₂ concentration, irrespective of climate state. The absence (EECO), or expansion (LGM) of continental ice sheets has the potential to affect the zonally averaged surface temperatures due to the lapse-rate effect (see Box 5.2), hence contributing to polar amplification. However, polar amplification is also suppressed in zonally averaged gradients of SST compared with terrestrial surface air temperature (Box 5.1, Figure 1), owing to the presence of high-latitude sea ice in the pre-industrial control,

(continued on next page)

Box 5.1 (continued)

which places a lower limit on SST. Global mean temperature estimates for these three past climates also imply an Earth system climate sensitivity to radiative perturbations up to two times higher than the equilibrium climate sensitivity (Lunt et al., 2010; Haywood et al., 2013) (see Section 5.3.1 and Box 12.2).

Polar amplification explains in part why Greenland Ice Sheet (GIS) and the West Antarctic Ice Sheet (WAIS) appear to be highly sensitive to relatively small increases in CO_2 concentration and global mean temperature. For example, global sea level during MPWP may have been up to +20m higher than present day when atmospheric CO_2 concentrations were ~350 to 450 ppm and global mean surface temperature was 2°C to 3°C above pre-industrial levels (see Sections 5.6.1 and 5.8.1). (continued on next page)



Box 5.1, Figure 1 | Comparison of data and multi-model mean (MMM) simulations, for four periods of time, showing (a) sea surface temperature (SST) anomalies, (b) zonally averaged SST anomalies, (c) zonally averaged global (green) and land (grey) surface air temperature (SAT) anomalies and (d) land SAT anomalies. The time periods are 2081–2100 for the Representative Concentration Pathway (RCP) 8.5 (top row), Last Glacial Maximum (LGM, second row), mid-Pliocene Warm Period (MPWP, third row) and Early Eocene Climatic Optimum (EECO, bottom row). Model temperature anomalies are calculated relative to the pre-industrial value of each model in the ensemble prior to calculating the MMM anomaly (a, d; colour shading). Zonal MMM gradients (b, c) are plotted with a shaded band indicating 2 standard deviations. Site specific temperature anomalies estimated from proxy data are calculated relative to present site temperatures and are plotted (a, d) using the same colour scale as the model data, and a circle-size scaled to estimates of confidence. Proxy data compilations for the LGM are from Multiproxy Approach for the Reconstruction of the Glacial Ocean surface (MARGO) Project Members (2009) and Bartlein et al. (2011), for the MPWP are from Dowsett et al. (2012), Salzmann et al. (2008) and Haywood et al. (2013) and for the EECO are from Hollis et al. (2012) and Lunt et al. (2012). Model ensemble simulations for 2081–2100 are from the CMIP5 ensemble using RCP 8.5, for the LGM are seven Paleoclimate Modelling Intercomparison Project Phase III (PMIP3) and Coupled Model Intercomparison Project Phase 5 (CMIP5) models, for the Pliocene are from Haywood et al., (2013), and for the EECO are after Lunt et al. (2012).

Box 5.1 (continued)

Based on earlier climate data–model comparisons, it has been claimed (summarised in Huber and Caballero, 2011), that models underestimated the strength of polar amplification for high CO₂ climates by 30 to 50%. While recent simulations of the EECO and the MPWP exhibit a wide inter-model variability, there is generally good agreement between new simulations and data, particularly if seasonal biases in some of the marine SST proxies from high-latitude sites are considered (Hollis et al., 2012; Lunt et al., 2012; Haywood et al., 2013).

Transient polar amplification as recorded in historical instrumental data and as projected by coupled climate models for the 21st century involves a different balance of feedbacks than for the “equilibrium” past states featured in Box 5.1, Figure 1. Since 1875, the Arctic north of 60°N latitude has warmed at a rate of 1.36°C per century, approximately twice as fast as the global average (Bekryaev et al., 2010), and since 1979, Arctic land surface has warmed at an even higher rate of 0.5°C per decade (e.g., Climatic Research Unit (CRU) Gridded Dataset of Global Historical Near-Surface Air TEMperature Anomalies Over Land version 4 (CRUTEM4), Jones et al., 2012; Hadley Centre/CRU gridded surface temperature data set version 4 (HadCRUT4), Morice et al., 2012) (see Section 2.4). This recent warming appears unusual in the context of reconstructions spanning the past 2000 years (Section 5.5) and has been attributed primarily to anthropogenic factors (Gillett et al., 2008) (see Section 10.3.1.1.4). The fact that the strongest warming occurs in autumn and early winter (Chylek et al., 2009; Serreze et al., 2009; Polyakov et al., 2010; Screen and Simmonds, 2010; Semenov et al., 2010; Spielhagen et al., 2011) strongly links Arctic amplification to feedbacks associated with the seasonal reduction in sea ice extent and duration, as well as the insulating effect of sea ice in winter (e.g., Soden et al., 2008; Serreze et al., 2009; Serreze and Barry, 2011). For future model projections (Box 5.1, Figure 1), following the RCP8.5 scenarios, annual mean Arctic (68°N to 90°N) warming is expected to exceed the global average by 2.2 to 2.4 times for the period 2081–2100 compared to 1986–2005 (see Section 12.4.3.1), which corresponds to the higher end of polar amplification implied by paleo-reconstructions.

The transient response of Antarctic and Southern Ocean temperatures to the anthropogenic perturbation appears more complex, than for the Arctic region. Zonal mean Antarctic surface warming has been modest at 0.1°C per decade over the past 50 years (Steig et al., 2009; O'Donnell et al., 2010). The Antarctic Peninsula is experiencing one of the strongest regional warming trends (0.5°C per decade over the past 50 years), more than twice that of the global mean temperature. Central West Antarctica may have also experienced a similar strong warming trend, as depicted by the only continuous meteorological station during the last 50 years (Bromwich et al., 2013), and borehole measurements spanning the same period (Orsi et al., 2012). Ice core records show enhanced summer melting in the Antarctic Peninsula since the 1950, which is unprecedented over the past 1000 years (Abram et al., 2013), and warming in West Antarctica that cannot be distinguished from natural variability over the last 2000 years (Steig et al., 2013) (see also Section 10.3.1.1.4, and Section 5.5). Polar amplification in the Southern Ocean and Antarctica is virtually absent in the transient CMIP5 RCP4.5 future simulations (2081–2100 versus 1986–2005) (see Section 12.4.3.1), although CMIP5 RCP8.5 exhibits an amplified warming in the Southern Ocean (Box 5.1, Figure 1), much smaller in magnitude than the equilibrium response implied from paleo-reconstructions for a high-CO₂ world.

In summary, *high confidence* exists for polar amplification in either one or both hemispheres, based on robust and consistent evidence from temperature reconstructions of past climates, recent instrumental temperature records and climate model simulations of past, present and future climate changes.

5.3 Earth System Responses and Feedbacks at Global and Hemispheric Scales

This section updates the information available since AR4 on changes in surface temperature on million-year to orbital time scales and for the last 2000 years. New information on changes of the monsoon systems on glacial–interglacial time scales is also assessed.

5.3.1 High-Carbon Dioxide Worlds and Temperature

Cenozoic (last 65 Ma) geological archives provide examples of natural climate states globally warmer than the present, which are associated with atmospheric CO₂ concentrations above pre-industrial levels. This relationship between global warmth and high CO₂ is complicated by

factors such as tectonics and the evolution of biological systems, which play an important role in the carbon cycle (e.g., Zachos et al., 2008). Although new reconstructions of deep-ocean temperatures have been compiled since AR4 (e.g., Cramer et al., 2011), *low confidence* remains in the precise relationship between CO₂ and deep-ocean temperature (Beerling and Royer, 2011).

Since AR4 new proxy and model data have become available from three Cenozoic warm periods to enable an assessment of forcing, feedbacks and the surface temperature response (e.g., Dowsett et al., 2012; Lunt et al., 2012; Haywood et al., 2013). These are the Paleocene–Eocene Thermal Maximum (PETM; Table 5.1), the Early Eocene Climatic Optimum (EECO; Table 5.1) and the mid-Pliocene Warm Period (MPWP; Table 5.1). Reconstructions of surface temperatures based on proxy data remain